# Joint adjustment of strain rate fields and its application in shallow seismicity forecast in the Sichuan-Yunnan region, China

Shuang Zhu[1] · Changyun Chen[1] · Wei Zhan[1] · Jingwei Li[1] · Nannan Guo[1] · Xuechuan Li[1] · Guangli Su[1]

**Abstract**
Calculation methods for large-scale strain rate fields from GNSS horizontal velocity can be divided into two types, namely mathematical and physical methods, which reflect different characteristics of the strain rate field. Therefore, it is necessary to combine these two types of methods to obtain a more reasonable strain rate field. In this study, strain rate fields made from the least-squares collocation (mathematical method) and fault model (physical method) were jointly processed by using Helmert variance component estimation, and the reliability of the joint results was analyzed based on the simulated and measured GNSS velocity. Then, the effect of station density on the strain rate field in the Sichuan-Yunnan region was analyzed, and the results show that the mathematical method was influenced by station density significantly. Based on the joint strain rate field in the Sichuan-Yunnan region, shallow seismicity forecast rates was calculated in conjunction with the Global Centroid-Moment-Tensor Earthquake Catalogue from 1976 to 2021. The results indicate that the shallow seismicity forecast rates of the Sichuan-Yunnan region is high, with 3 Mw≥7.0 earthquakes may occur every 100 years.

**Keywords** Strain rate · Least-squares collocation method · Fault model · Helmert variance component estimation · Shallow seismicity forecast

## 1 Introduction

Large-scale strain rate field are widely used for describing crustal deformation characterization because they do not rely on a reference frame and reflect deformation information directly (McCaffrey 2005; Parsons 2006; Shen et al. 2007). The strain rate field can be used to identify the deformation characteristics of the crust before a strong earthquake, determine

✉ Changyun Chen
ccy_666@163.com

1    The First Monitoring and Application Center, CEA, Tianjin 300180, China

the characteristics of the deformation field, and ascertain the proportion of elastic strain in the total accumulated strain, which is directly related to the nucleation of strong earthquakes (Li et al. 2022; Wang and Shen 2020; Wu et al. 2022). The strain rate field provides an understanding of earthquake preparation and facilitates advancing earthquake prediction research (Riguzzi et al. 2012; Zeng et al. 2018; Zheng et al. 2018; Guo et al. 2022; Pang 2022; Zhang et al. 2022). However, there are multiple methods to calculate strain rates, which produce different results for the same source data. It is crucial to obtain a reliable strain rate field.

Strain rate calculation methods from GNSS horizontal velocity can be divided into mathematical and physical methods. Mathematical methods construct equations to solve the strain (rate) distribution directly, mainly based on the differential relationship between the strain rate and displacement and their graded spreads (Li et al. 2001; Hsu et al. 2009; Yu and Lu 1978). It has the advantages of better description of the observed data, simplicity of calculation, and suitability for describing continuous deformation (Tape et al. 2009; Jiang and Liu 2010). The differences between the four mathematical methods (least-squares collocation, spherical harmonic function, polyhedral function, and Delaunay triangle methods) have been compared systematically based on simulated and measured data, providing an evaluation of their edge effects, reliability, applicability, and resistance to discrepancies (Wu et al. 2011; Wu 2012). In addition to the mathematical relationship between strain (rate) and displacement (velocity), the physical methods also consider the effects of the fault and medium parameters in the study area, mainly including the fault model and numerical simulation methods (Bird 2009; Savage and Burford 1973). These methods are mainly suitable for regions where a main fault exists in the study area and the medium parameters are relatively clear.

The mathematical method is generally aimed at describing the observed data, but it does not focus on whether the deformation is caused by faults, neither does it consider whether the strain is generated by the main faults in the study area, by branching faults within the block, or by continuous deformation of the block. It is also more difficult to reflect the rapid deformation near the faults using the approach. The physical method considers the most dominant strains in the study area to be caused by faults and assumes the deformation within the block to be very weak or even negligible, resulting in high strain rates calculated near the faults and rapid decay of strain rates away from the faults. To obtain the strain rate field results of the Sichuan-Yunnan region of China accurately, we use Helmert variance component estimation to jointly process strain rate field results given by the least-squares collocation (mathematical method) and fault model methods (physical method) (Helmert 1907; Kotsakis and Sideris 1999; Cui et al. 2009; Xu and Liu 2014). The mathematical method is difficult to highlight the fracture deformation characteristics when there are few stations, while the joint method can improve the calculation ability of strain near the fault effectively. Based on this, the joint strain rate field results were used to estimate shallow seismicity forecast rates in the Sichuan-Yunnan region based on the SHIFT assumption and algorithm (Bird and Kreemer 2015; Zheng et al. 2018), and the seismic hazard was analyzed.

## 2 Methods

Regional crustal deformation and strain distribution based on geodetic observations are important in the analysis of the physical processes of strong earthquakes. We selected a representative mathematical method (least-squares collocation) (Jiang and Liu 2010; Wu et al. 2011) and a physical method (fault model) (Okada 1985) to objectively describe the Global Navigation Satellite System (GNSS) strain rate distribution in the study area.

### 2.1 Least-squares collocation

The least-squares collocation method has been discussed in detail in previous studies (Heiskanen and Moritz 1967; Yu and Lu 1978). The following Eq. (1) gives a direct solution. In the formula, $\widehat{Z}$ is the estimation of random signals (including observation and estimation values), $G$ is the coefficient matrix of the classical adjustment, $\hat{Y}$ is the undetermined parameter to be solved in the classical adjustment, $L$ are the observed values, $D_X$ is the covariance matrix of measured points signals, $D_Z$ is the covariance matrix of all points signals, $D_\Delta$ is the covariance matrix of observed values.

$$\begin{cases} \widehat{Y} = \left\{ G^T(D_X + D_\Delta)^{-1}G \right\}^{-1} G^T(D_X + D_\Delta)^{-1}L \\ \widehat{Z} = D_Z(D_X + D_\Delta)^{-1}\left( L - G\widehat{Y} \right) \end{cases} \tag{1}$$

When Eq. (1) is used to describe large-scale crustal movements, the covariance distribution of signals should be determined first. Previous studies have discussed the covariance distribution of signals in depth (Jiang and Liu 2010; Wu et al. 2011), this study used the Gaussian covariance function, as shown in Eq. (2).

$$f(d) = Ae^{-k^2d^2} \tag{2}$$

In Eq. (2), $A$ and $k$ are parameters to be determined, which can be obtained statistically. A relationship between the covariance and the distance $d\,(\text{km})$ can be established, $d$ can be expressed as a function of the geodetic coordinates $(\lambda, \varphi)$ on the sphere. The displacement field of the study area can be expressed as a function of the point position $(\lambda, \varphi)$ using Eq. (2), and the strain results on the sphere can be obtained according to the differential relationship between displacement and strain.

### 2.2 Fault model

Savage and Burford (1973) provided a displacement formula for the interseismic deformation curve of a strike-slip fault by means of a 'spiral' dislocation: the inverse tangent function. Okada (1985) summarized and deduced the dislocation formula under a semi-infinite space uniform medium, and described the relationship between fault slip and surface displacement, strain, and strain gradient. The Okada fault model is based on a finite rectangular surface, and the representation of surface deformation and strain can be obtained by integrating the point-source dislocation expressions over the rectangular surface. It is a complex

theoretical equation suitable for calculating displacement, strain, and tilt deformation due to any shear and tensile fault.

The geometric relation of the fault model is shown in Fig. 1. The elastic medium is filled with the region z≤0 (that is, semi-infinite space), the axis parallel to the strike of the fault is taken as the X-axis, and the dislocation components U1, U2 and U3 respectively correspond to the strike-slip, dip-slip and extensional dislocation components of any dislocation. δ is the dip angle of the fault plane, d represents the focal depth, and L and W respectively represent the length and width of the fault.

The distribution of the strain field can be obtained based on the fault slip rate within the study area using the fault model. The strain rate field is obtained in two main steps: (1) calculating the slip rates of the main fault based on the GNSS horizontal velocity and (2) calculating the strain rate distribution due to fault slip. Blocks software(Meade and Hager 2005)was used to calculate the slip rate. The relevant locking depth information of the fault was sourced from previous research (Shen et al. 2005; Wang et al. 2008; Li et al. 2021). For the fault zones where no relevant research results were available, a unified locking depth of 15 km was used based on the results of precise relocation of small earthquakes and the crustal structure in Sichuan-Yunnan region (Zhao 2012; Zhang 2019). Subsequently, the surface strain rate distribution results were calculated by the fault model using the fault slip rate. We assumed that Lamé parameters are equal ($\lambda = \mu$), the medium constant in the Okada model is 0.667 (Okada 1985). The Okada model was used to calculate the strain in the fault model method.

## 2.3 Helmert adjustment

Both Mathematical and physical methods have advantages as well as disadvantages. The mathematical method can describe strain changes over a wide range of deformation fields but does not highlight the rapid changes in the region near the faults, and the physical method focuses on describing discontinuous changes near the faults but encounters difficulties with strains in the far field.

To obtain a more accurate strain rate field, we developed a joint adjustment method using Helmert variance component estimation to process mathematical and physical results. First, we fitted the results of the two computational methods using a multi-surface function fitting method, which was proposed by Hardy in 1978 and has been recommended for crustal deformation analysis in the USA (Hardy 1978). In this study, the multi-surface function was improved by constructing a functional model containing a first-order plane function plus a step term, as shown in Eq. (3), and the kernel function was constructed as shown in

**Fig. 1** Okada fault model
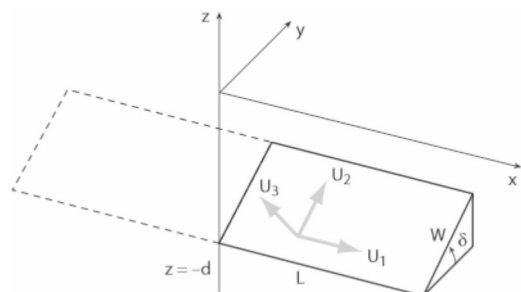
Eq. (4). $x_i$ and $y_i$ are latitude and longitude of the station. The values of parameters $k$ and $a$ should be determined first, which can be obtained statistically (Jiang and Liu 2010; Wu et al. 2011). Then, based on the principle of indirect adjustment, the equation can be solved for the parameters, and the error estimates can be obtained.

$$v_i = A + Bx_i + Cy_i + Dx_i^2 + Ey_i^2 + Fx_iy_i + g\,(0\ or\ 1)\,+$$

$$\sum_{j=1}^{n} a_jQ(\lambda_i, \varphi_i, \lambda_j, \varphi_j) - L_i \tag{3}$$

$$Q(\lambda, \phi, \lambda_j, \phi_j) = e^{-(kd_{(\lambda,\phi,\lambda_j,\phi_j)}^2)^a} \tag{4}$$

The strain results calculated by the two different methods can be expressed as a function of latitude and longitude by using Eqs. (3) and (4). Since the stations of two different methods are different, the results are interpolated to make the longitude and latitude of the two results completely consistent, and then the joint adjustment is carried out.

Owing to the different error compositions of the two methods, Helmert variance component estimation was used to determine weighting. The basic process was as follows: (1) Two sets of error equations and weight matrices $P_1, P_2$ were established based on Eq. (3), then the normal equations were formed and solved. (2) Parameters $\theta_1$ and $\theta_2$ were solved according to Eq. (5). 3)We determined whether $|\theta_1/\theta_2 - 1| < \epsilon$ was satisfied, where $\epsilon$ is 0.01. If satisfied, iteration was halted, otherwise, $P_2^{new} = P_2^{old} * \left(\frac{\theta_1}{\theta_2} - 1\right)$ to modify the second weight matrix. Steps 1–3 were repeated until the iteration stopped, and the weight matrix was obtained. Using this method, the weights of the two strain calculation methods can be modified to form a new normal equation for a unified solution, resulting in a joint adjustment of the two methods (Wu et al.2021).

$$\begin{bmatrix} n_1 - 2tr\left(N_1N^{-1}\right) + tr\left(N_1N^{-1}N_1N^{-1}\right) & tr\left(N_1N^{-1}N_2N^{-1}\right) \\ tr\left(N_1N^{-1}N_2N^{-1}\right) & n_2 - 2tr\left(N_2N^{-1}\right) + tr\left(N_2N^{-1}N_2N^{-1}\right) \end{bmatrix} \begin{bmatrix} \theta_1 \\ \theta_2 \end{bmatrix} = \begin{bmatrix} V_1^TP_1V_1 \\ V_2^TP_2V_2 \end{bmatrix} \tag{5}$$

where $\theta_1$ and $\theta_2$ are posterior variances of the strain rate of the two strain results, $P_1, P_2, V_1$ , and $V_2$ are the corresponding equation matrices; $N_1 = B_1^TP_1B_1$ and $N_2 = B_2^TP_2B_2$ are the arrays of equation coefficients for the two strain datasets; $N = B^TPB$ is the array of Helmert adjustment equation coefficients; $n_1, n_2$ are the number of error equations; and $tr\,(M)$ denotes the trace of the matrix $M$.

# 3 Joint adjustment of strain rate field

## 3.1 Joint result based on simulated velocity

In this study, the Sichuan-Yunnan region (99°E–105°E, 24°N–33°N) was selected to implement the Helmert adjustment. First, the simulated velocity was generated by Eq. (6) and Eq. (7), where $f_n(\lambda, \varphi)$ and $f_e(\lambda, \varphi)$ represent the continuous deformation components, and $g_{ni}(\lambda, \varphi)$ and $g_{ei}(\lambda, \varphi)$ are the fault deformation components (see Fig. 2(a) for the exact location of the fault). The data of three simulated faults was based on the geometric

trend, strike slip velocity, and locking depth of the Xianshuihe-Xiaojiang fault in this region. To render the velocity field more complicated, we added the extra exponential functions in $f_n(\lambda, \varphi)$ and $f_e(\lambda, \varphi)$. The data simulation formula in Wu et al. (2017) was used as a reference in this study. $\lambda$ represents longitude, $\varphi$ represents latitude (in radians), $\nabla\lambda_i$ and $\nabla\varphi_i$ denote the difference between the measured point and the projected point on the fault, and $rand()$ is the additional white noise. Figure 2(a) shows the simulated velocity field results for the Sichuan-Yunnan region based on the generation model with an additional error of $\pm 1.5$ mm/a.

Based on the velocity field formula, Eq. (8) can be used to calculate the theoretical strain parameters, which in turn obtaining theoretical strain results.

$$\begin{cases} v_n = f_n(\lambda, \varphi) + g_{n1}(\lambda, \varphi) + g_{n2}(\lambda, \varphi) + g_{n3}(\lambda, \varphi) + rand() \\ v_e = f_e(\lambda, \varphi) + g_{e1}(\lambda, \varphi) + g_{e2}(\lambda, \varphi) + g_{e3}(\lambda, \varphi) + rand() \end{cases} \quad (6)$$

$$\begin{cases} f_n(\lambda, \varphi) = 15sin(4\lambda^2)cos(3\varphi^2) + 5.0 \times 1.2^{\lambda\varphi} - 4.0 \times 1.3^{\lambda\varphi} + 0.5\lambda^2 - 2\varphi^2 \\ f_e(\lambda, \varphi) = 18sin(3\lambda^2)cos(4\varphi^2) + 5.0 \times 1.5^{\lambda\varphi} - 4.0 \times 1.7^{\lambda\varphi} + \lambda^2 - 1.5\varphi^2 \\ \\ g_{n1}(\lambda, \varphi) = 3.5arctan(120 \times \nabla\lambda_1) \\ g_{e1}(\lambda, \varphi) = -3.5arctan(120 \times \nabla\varphi_1) \\ \\ g_{n2}(\lambda, \varphi) = 9.0arctan(60 \times \nabla\lambda_2) \\ g_{e2}(\lambda, \varphi) = -3.5arctan(60 \times \nabla\varphi_2) \\ \\ g_{n3}(\lambda, \varphi) = 4.0arctan(80 \times \nabla\lambda_3) \\ g_{e3}(\lambda, \varphi) = 1.2arctan(80 \times \nabla\lambda_3) \end{cases} \quad (7)$$

$$\begin{cases} \epsilon_\varphi = \frac{1}{R}\frac{\partial u_\varphi}{\partial \varphi} \\ \epsilon_\lambda = \frac{1}{Rcos\varphi}\frac{\partial u_\lambda}{\partial \lambda} - \frac{u_\varphi}{R}tan\varphi \\ \epsilon_{\lambda\varphi} = \frac{1}{2}[\frac{1}{Rcos\varphi}\frac{\partial u_\varphi}{\partial \lambda} + \frac{u_\lambda}{R}tan\varphi + \frac{1}{R}\frac{\partial u_\lambda}{\partial \varphi}] \end{cases} \quad (8)$$

Where R is the average radius of curvature, and $\varepsilon_\phi$, $\varepsilon_\lambda$ and $\varepsilon_{\lambda\phi}$ are strain tensors.

Simulated faults 1, 2 and 3 were pure strike-slip faults with dip angle of 90°. The strike and length of faults were calculated using the latitude and longitude of the two ends of the fault. GNSS profiles were used to calculate the slip rate of the faults then the fault model was used to calculate the strain of the simulated velocity field. First, we created a GNSS profile on the fault, calculated the average velocity on both sides of the profile and subtracted those two values to derive the fault's slip rate value, the GNSS profiles' location were showed in Fig. 2(a), profiles results are given in Supplementary file1. Then the arctangent model was used to invert the locking depth of the fault (Paul 2010), and the finally strain was calculated based on these parameters. Based on this simulated velocity, the strain rate field was calculated by using least-squares collocation, the fault model, and Helmert adjustment, as shown in Fig. 2. The difference between calculation strain results and theoretical values is shown in Fig. 3.

The results calculated by the least-squares collocation method (Fig. 2c) reflected the high strain value near the fault and showed variations in the region away from the fault, which was close to the spatial characteristics of the theoretical value (Fig. 2b). The results from the fault model (Fig. 2d) were concentrated in the near-fault region, and disappeared rapidly with increasing distance from the fault. The joint strain rate (Fig. 2e) showed both the high strain values on the fault and low strain values in the region away from the fault, which was closer to the theoretical values (Fig. 2b). The difference between joint strain results and theoretical values was smaller than the least-squares collocation result and fault model result.
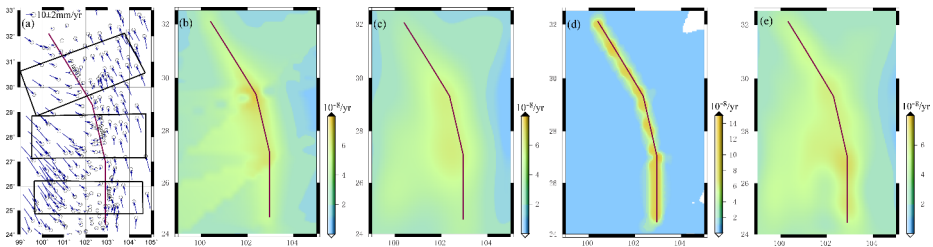


**Fig. 2** Simulated velocity field and maximum shear strain field results of the Sichuan-Yunnan region: **a** simulated velocity field, **b** theoretical strain results, **c** results of least-squares collocation methods, **d** results of fault model, and **e** results of Helmert adjustment
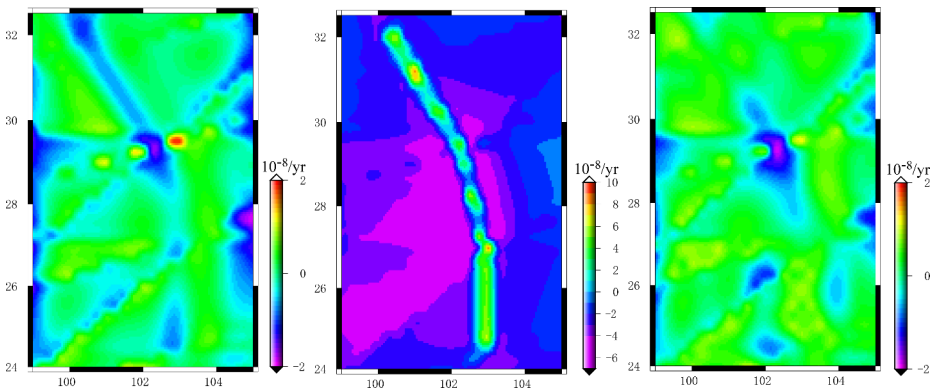


**Fig. 3** Difference between calculated strain results and theoretical values: **a** difference between results of least-squares collocation methods and theoretical values, **b** difference between results of fault model and theoretical values, and **c** difference between results of Helmert adjustment and theoretical values

The agreement between the calculated results and theoretical values was analyzed from the perspective of correlation. The correlation coefficients between the calculated results and theoretical results were calculated according to the correlation coefficient formula (Wu et al. 2011). The range of the strain rate for correlation coefficients calculation was slightly smaller than the range of the actual input data to reduce the influence of edge effects. The results showed that the joint strain results were relatively close to the theoretical values, with a correlation coefficient distribution of 0.91–0.97. The least-squares collocation method had a correlation coefficient distribution of 0.89–0.93, and the joint strain field was closer to the theoretical strain rate field.

**Fig. 4** Slip rate of main faults in Sichuan-Yunnan region: **a** results of strike-slip rate, and **b** results of tension rate
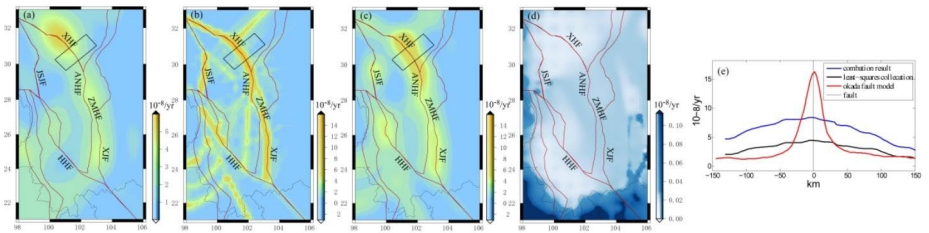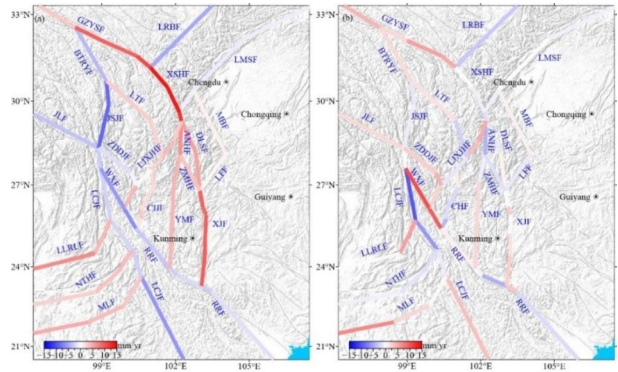




**Fig. 5** Maximum shear strain field results: **a** results of least-squares collocation method, **b** results of fault model, **c** results of Helmert adjustment, **d** error distribution of Helmert adjustment, and **e** comparison of strain field results obtained using different methods

## 3.2 Joint result based on observed velocity

Based on the observed velocity in the Sichuan-Yunnan region (Wang and Shen 2020), the maximum shear strain rate in the Sichuan-Yunnan region were calculated by the least-squares collocation method and fault model method. The fault distribution in this region as generated by the fault model method was considered, and the slip rate of major faults was estimated with Blocks software. First, fault location and locking degree were used with Blocks to calculate the slip rate of the fault (Shen et al. 2005; Wang et al. 2008; Li et al. 2021), then, the fault slip rate was used as the driving force, and the strain rate caused by fault slip was calculated by the fault model. The slip rates of major faults estimated by Blocks software were showed in Fig. 4. The locking depth is an important parameter. Locking depth estimates exist for all the highly studied active fault zones in the region, such as the Ganzi-Yushu- Xianshuihe-Xiaojiang fault system, Daliangshan fault system, Longmenshan Red River fault system, Red River fault system and Lijiang-Xiaojinhe fault system, therefore the relevant research results were used. As described above, a unified value of 15 km was used for the fault zones without locking depth information (Zhao 2012; Zhang 2019). Table of main faults information is given in Supplementary file2. The joint results of maximum shear strain rate in the Sichuan-Yunnan region were obtained by Helmert adjustment of the least-squares collocation and fault model methods, as shown in Fig. 5.

The high values obtained using the least-squares collocation (Fig. 5a) were concentrated in the near-fault areas, such as the Xianshuihe-Anninghe-Zemuhe-Xiaojiang Fault, while

the strain results in the near-fault areas and within the block exhibited less variation. The high values obtained using the fault model (Fig. 5b) were also concentrated in the near-fault areas, however, these values were generally higher than those of the least-squares collocation method, and the change between the main fault and the interior of the block was more drastic. The joint strain field (Fig. 5c) retained the spatial characteristics of the least-squares collocation results; however, the strain values in the near-fault area were higher and closer to the fault model results. This suggests that the Helmert adjustment can combine the advantages of both mathematical and physical methods of strain field calculation, by integrating the rapid deformation near the main faults and the slow deformation characteristics within the block to obtain more realistic strain rate results. The errors in the joint results (Fig. 5d) were generally reduced, with high values being concentrated only at the southern edge of the study area.

Compared with the results obtained using a single method, the most significant differences in the Helmert adjustment were mainly in the high-value zone of the Xianshuihe-Anninghe faults, which were somewhat elevated. To verify the results of the strain calculations, a GNSS profile was created for the Xianshuihe fault zone and its maximum shear strain results were calculated, as shown in Fig. 5(e). The fault model indicated that the strain was mainly caused by the fault, resulting in a large strain rate of $16\times10^{-8}$/yr on the fault, which decayed rapidly away from the fault. In contrast, the least-squares collocation method had a value of $3.86\times10^{-8}$/yr near the fault. The mathematical model is focused on describe the observed data well and does not generally focus on whether the deformation is caused by the fault, values in the fault zone were relatively larger than those away from the fault. However, the difference was not significant and decayed slowly, not reflecting the rapid deformation near the fault. After Helmert adjustment, the value was $6.34\times10^{-8}$/yr, and the strain value near the fault was significantly higher. In the mathematical model, the spatial distribution of stations near the fault was not sufficient to constrain high strain rate results, and strain rates near the fault can be underestimated due to the model errors. However, the fault model assumed that all strains were generated by the main fault, ignoring the role of partial branching faults or internal deformation within the block. The differences between the two methods can be accommodated in the Helmert adjustment method, allowing the advantages of both the mathematical method and the fault model to be incorporated, which results in a more accurate description of strain distribution.

Another difference was observed in the Jinshajiang fault. Because of the low station density in the zone, the mathematical model encountered difficulties in accurately describing the local deformation model, resulting in the strain results calculated by least-squares collocation to be smaller in the area. In contrast, the deformation caused by the fault was emphasized in the fault model, and those strain results for the Jinshajiang fault were higher. The lack of observations can be compensated when using the joint adjustment method, allowing accurate representation of the strain.

## 4 Shallow seismicity forecast

The maximum shear strain rate calculated by Helmert adjustment was shown in Fig. 5(c). The eastern boundary of the Sichuan-Yunnan block was significantly higher than that of other regions, indicating that the Xianshuihe-Xiaojiang fault system at the eastern boundary

of the Sichuan-Yunnan block dominates the regional deformation. The highest maximum shear strain value, in excess of $16 \times 10^{-8}$/yr, was present in the NW segment of the Xianshuihe fault zone and the slip rate of the Xianshuihe fault was high under the effect of higher shear strain. The shear strain of the Honghe Fault Zone, one of the large structures in the region, was significantly lower. With the exception of the eastern boundary of the Sichuan-Yunnan region, shear strain values of the southwestward extension of the Xiaojiang Fault and Jinshajiang Fault Zones, the southeastern section of the Lancangjiang Fault Zone, the Chenghai Basin, and nearby areas, were relatively high, whereas the shear strain values of the Lancangjiang and Longmenshan Fault were low.

Using the joint strain field results and the Global Centroid Moment Tensor (GCMT) Catalog of 1976–2021(http://peterbird.name/oldFTP/Seismicity/), shallow earthquakes were predicted based on the SHIFT assumption and using the SHIFT_GSRM2f program developed by Bird et al. (2010,2015). The SHIFT assumption converts seismic moment rates into long-term seismic predictions along tectonic faults based on frequency/magnitude relationships for the most similar plate boundary types. Seismic moment rates of tectonic faults can be calculated from the strain rate and mean coupled seismic thickness of the most similar plate boundary types (Bird and Kreemer 2015). We used the PB2002 rigid plate model, plate boundary assignment rule, and other necessary parameters established by Bird as inputs to calculate the predicted shallow earthquakes in the Sichuan-Yunnan region (Bird 2003).

The occurrence of 3 shallow earthquakes of $Mw \geq 7.0$ every 100 years was predicted, and Fig. 6(a) is the forecast result obtained based on the joint results, Fig. 6(b) is the forecast result obtained based on the strain results of the least-squares collocation method. We performed a consistency check of the Helmert adjustment forecast results against the seismic catalog used in the forecast. We counted the earthquakes in different magnitude ranges in the 1976–2021 GCMT catalog and then normalized the numbers to 100-year timescale, shown as blue circles in Fig. 6c. We found that our forecast results based on this seismic catalog
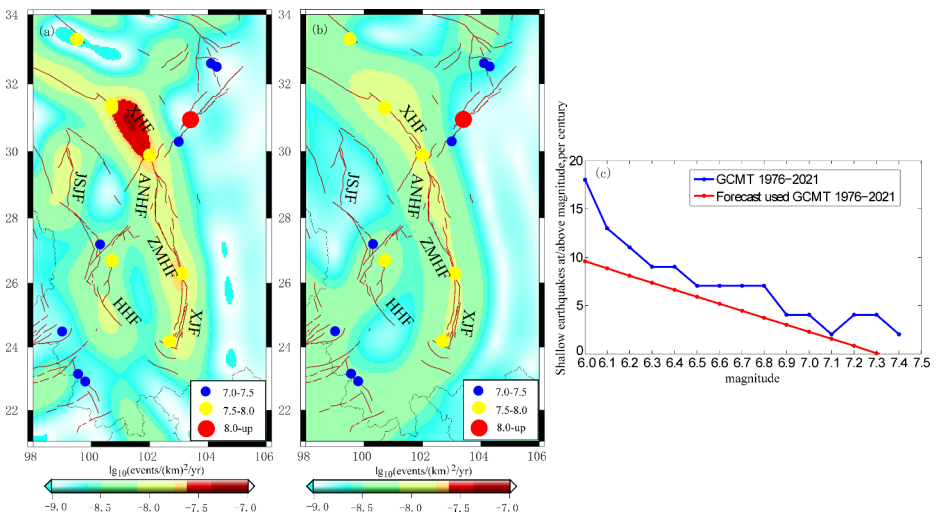


**Fig. 6** Forecast result of the shallow seismicity in the Sichuan-Yunnan region: **a** results based on Helmert adjustment strain, **b** results based on strain of least-squares collocation methods, and **c** quality assessment of forecast results based on Helmert adjustment strain, colored dots in **a** and **b** represent earthquakes in the 1976–2021 GCMT catalog

(shown as red circles in Fig. 6c), were in good agreement with them. The non-parametric Kendall coordination coefficient of the W test was applied to these two sets of 'magnitudes-times' and a Kendall's -W coefficient of 0.943, indicated a good agreement.

The highest values obtained based on the joint strain were mainly distributed in the Xianshuihe-Xiaojiang fault zone, followed by the Jinshajiang fault zone. Compared with the forecast results of the least-squares collocation method and the results of previous studies (Zhan et al. 2021), a significant difference in shallow earthquake forecast calculated by the joint strain field was present in the Jinshajiang Fault Zone, where the value near the Jinshajiang fault has improved from −9.0 to -8.4. This was because the strain results of the fault model were integrated into the Helmert adjustment strain result, making up for the defects in observed data density from using only mathematical methods. The joint result highlighted the accumulation of the strain near the Jinshajiang fault, thus improving the forecast quality for this fault zone.

In addition, two main factors influenced the earthquake forecast. The first was the spatial resolution of the geodetic survey. As the geodetic spatial resolution increases, the strain rates and raw seismic moment rates calculated based on the regular grid also become more detailed and accurate. The second was the completeness and reasonableness of the GCMT seismic catalog, which was used to optimize the empirical constants. The completeness of the collected statistics and the accuracy and reasonableness of the classification of the GCMT calculations have an important impact on the reliability of seismic predictions. With the accumulation of seismic events and the optimization of the GCMT calculation, the GCMT seismic catalog continues to become more complete, robust, and reasonable, which improves the robustness of earthquake predictions.

The seismic hazard of the study area can be reflected by the seismic forecast results. It was evident from the different forecast results that the Xianshuihe-Xiaojiang fault zone was the most significantly deformed region in the Sichuan-Yunnan region, with higher strain rates throughout the fault zone, and that were significantly higher than those of the surrounding areas. Previous studies have defined four seismic hollow zones along this fault zone (Wen et al. 2008; Shan et al. 2003), and the Daofu-Kangding seismic hollow zone experienced the Kangding Mw 5.9 earthquake in 2014. However, its magnitude was small, and the energy released was much lower than the energy accumulated (Jiang et al. 2015). Therefore, the seismic hazard of this seismic hollow remains high.

## 5 Discussion

Owing to geological structures and topographic and construction conditions, GNSS stations were not distributed randomly, and the strain rate results obtained from different velocities were also varied. For this reason, the velocity fields of the increased stations were generated based on the theoretical formula, and the strain rate results were compared. In this study, the Sichuan-Yunnan region (99°E–105°E, 24°N–33°N) was selected for analyzing of the effect of station density on the strain results calculated using the mathematical method. Figure 7(a) shows the velocity fields based on the increased observation stations compared to the velocity in Fig. 2(a). Because the fracture zone in the Sichuan-Yunnan region is mostly dominated by slip motion, the maximum shear strain results were selected for comparison in this study, and Fig. 7(b) shows the theoretical maximum shear strain rate field.

The results of the maximum shear strain rate obtained using the least-squares colloca-tion method, based on the two different velocity fields, as in Fig. 2(a) and Fig. 7(a), are presented in Fig. 7(c) and Fig. 7(d), respectively. In general, both strain fields reflected the shear deformation characteristics of the study area, with higher value around the main fault. In contrast to the theoretical results, the results showed some higher local values (different from the theoretical results), such as those in the southeast and southwest corner of the study area in Fig. 7(c). These deviations from the theoretical values were caused by the uneven distribution of stations and random errors. Compared with the results in Fig. 7(c), those in Fig. 7(d) were closer to the theoretical result. Similarly, the maximum shear strain showed better conformity with the theoretical results, with minor differences in the specific patterns.

The results show that an increase in the number of stations had no significant effect on the overall distribution of strain rate in the study area, however, the ability to discriminate the deformation in the fault zone was significantly improved. Owing to the low density of stations, the strain rate was localized, with higher values in the non-near-fault areas. It is notable that the local migration phenomenon of strain rate results was significantly decreased after adding additional stations, and that the high values were concentrated in the near-fault areas, indicating that the increment of stations can improve the reliability of the strain rate results. The correlation coefficients between the calculated and theoretical results were calculated according to the correlation coefficient formula (Wu et al. 2011). The strain results observed after an increasement in the number of stations were closer to the theoreti-cal values, with the correlation coefficient distribution (0.92–0.97) being comparable to that observed with the original stations (0.88–0.93). The strain rate results of the GNSS profiles also showed an overall increase near the fault area after increasing the number of stations, indicating that the density of stations had a greater influence on the strain rate results in the near-fault area. These comparisons indicate that the density of stations plays a key role in the mathematical calculation of strain rate since mathematical methods are more focused on describing the observed data well, and the station density affects the accuracy of strain calculation.

A comparative analysis of the Helmert adjustment method with different station densi-ties were performed, the joint strain results after an increasement of stations were similar
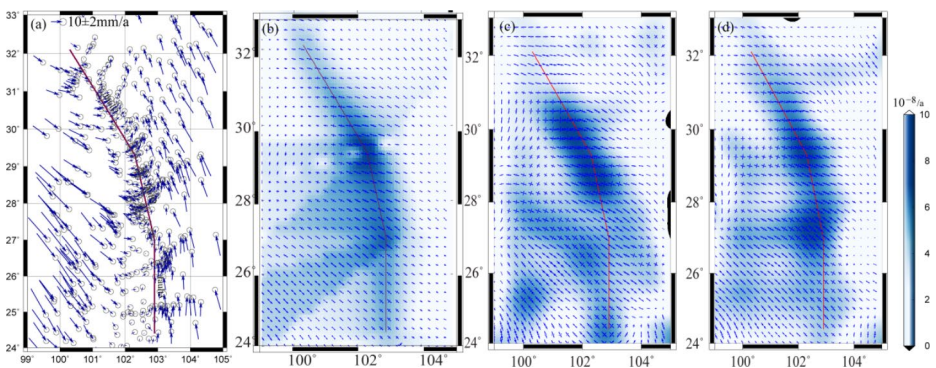


**Fig. 7** Simulated velocity and maximum shear strain rate fields calculated based on different station densi-ties: **a** Simulated velocity field based on increased stations, **b** theoretical maximum shear strain rate field, **c** maximum shear strain calculated based on original stations, and **d** maximum shear strain rate calculated based on the increased stations

to the original joint results, with the correlation coefficient distribution (0.92–0.98) being comparable to joint results with the original stations (0.91–0.97). Therefore, the Helmert adjustment of the mathematical and physical methods can compensate for an insufficient station density.

# 6 Conclusions

(1) Strain rate fields from GNSS horizontal velocity by using mathematical and physical methods reflect different characteristics of crustal deformation. A comparison of strain rate fields based on the simulated data showed that station density plays a key role in the mathematical method, which affects the accuracy of the strain rate fields. In contrast, the physical methods can compensate for the loss of deformation due to insufficient station density.

(2) To obtain more accurate strain results and better respond to the fault motion state, Helmert variance component estimation was proposed for the joint adjustment of mathematical and physical methods. The joint adjustment of the least-squares collocation method and fault model was performed using the simulated and actual measured data in the Sichuan-Yunnan region, and the joint results were analyzed by profile to confirm their validity, which reflected both rapid deformation in the near-fault area and continuous deformation inside the block. Furthermore, the joint results can compensate for the disadvantage that the mathematical method is difficult to highlight the fracture deformation characteristics when there are few stations, and improve the calculation ability of strain near the fault effectively, which provides a background basis for subsequent studies of crustal motion.

(3) The results of the joint strain field in the Sichuan-Yunnan region showed that the maximum shear strain at the eastern boundary of the Sichuan-Yunnan block was significantly higher than that in other regions. This indicated that the Xianshuihe–Xiaojiang fault system at the eastern boundary of the Sichuan-Yunnan block dominates the regional deformation, with the highest maximum shear strain value in the northwest section of the Xianshuihe fault zone. Based on the joint strain fields, combined with the Global CMT earthquake catalogue from 1976 to 2021, 3 Mw ≥ 7.0 earthquakes are predicted to occur in the Sichuan-Yunnan region every 100 years based on SHIFT assumptions and algorithms, and the Xianshuihe-Xiaojiang fault zone has a high seismic hazard.

**Author contributions** methodology, Shuang Zhu and Changyun Chen; formal analysis, Shuang Zhu and Changyun Chen; strain calculation, Wei Zhan, Jingwei Li; plotting figures, Nannan Guo, Xuechuan Li, Guangli Su; writing and editing, Shuang Zhu and Changyun Chen.

## Declarations

**Conflict of interest** The authors declare no conflict of interest.

# References

Bird P (2003) An updated digital model of plate boundaries. Geochem Geophys Geosyst 4(3):1027. https://doi.org/10.1029/2001GC000252

Bird P (2009) Long-term fault slip rates, distributed deformation rates, and forecast of seismicity in the western United States from joint fitting of community geologic, geodetic, and stress direction datasets. J Geophys Res Atmospheres 114(B11):292–310. https://doi.org/10.1029/2009JB006317

Bird P, Kreemer C (2015) Revised tectonic forecast of global shallow seismicity based on version 2.1 of the global strain rate map. Bull Seismol Soc Am 105(1):152–166. https://doi.org/10.1785/0120140129

Bird P, Kreemer C, Holt WE (2010) A long-term forecast of shallow seismicity based on the global strain rate map. Seismol Res Lett 81(2):184–194. https://doi.org/10.1785/gssrl.81.2.184

Bird P, Jackson DD, Kagan YY, Kreemer C, Stein RS (2015) GEAR1: a global earthquake activity rate model constructed from geodetic strain rates and smoothed seismicity. Bull Seismol Soc Am 105(5):2538–2554. https://doi.org/10.1785/0120150058

Cui XZ, Yu ZC, Tao BZ, Liu DJ, Yu ZL, Sun HY, Wang XZ (2009) Adjustment in surverying, 2nd edn. Wuhan Technical University of Surveying and Mapping Press, Wuhan

Guo NN, Wu YQ, Zhang QY (2022) Coseismic and pre-seismic deformation characteristics of the 2022 Ms6.9 Menyuan earthquake, China. Pure Appl Geophys 179:3177–3190. https://doi.org/10.1007/s00024-022-03128-3

Hardy RL (1978) The application of multi-quadric equations and point mass anomaly models to crustal movement studies. NOAA Technical Report NGS 76 NGS 11

Heiskanen WA, Moritz H (1967) Physical geodesy. Freeman and Company, San Francisco

Helmert FR (1907) Scientific books: die Ausgleichungsrechnung nach der Methode der kleinsten Quadrate, Zweite edn. Teubner, Leipzig

Hsu YJ, Yu SB, Simons M, Kuo LC, Chen HY (2009) Interseismic crustal deformation in the Taiwan plate boundary zone revealed by GPS observations, seismicity, and earthquake focal mechanisms. Tectonophysics 479(1–2):4–18. https://doi.org/10.1016/j.tecto.2008.11.016

Jiang ZS, Liu JN (2010) The method in establishing strain field and velocity field of crustal movement using least squares collocation. Chinese Journal of Geoplysics 2010, 53(5):1109–1117. https://doi.org/10.1002/cjg2.1507(In Chinese with English abstract)

Jiang G, Wen Y, Liu Y, Xu X, Fang L, Chen G, Gong M, Xu C (2015) Joint analysis of the 2014 Kangding, southwest China, earthquake sequence with seismicity relocation and InSAR inversion. Geophys Res Lett 42(9):3273–3281. https://doi.org/10.1002/2015GL063750

Kotsakis C, Sideris MG (1999) On the adjustment of combined GPS/levelling/geoid networks. J Geod 73(8):412–421. https://doi.org/10.1007/s001900050261

Li YX, Huang C, Hu XK, Shuai P, Hu XG, Zhang ZF (2001) The grid and elastic-plastic model of the blocks in intro-plate and strain status of principal blocks in the continent of China. Acta Seismol Sin 23(6):565–572 (In Chinese with English abstract)

Li YH, Hao M, Song SW, Zhu LY, Cui D, Zhuang WQ, Yang F, Wang QL (2021) Interseismic fault slip deficit and coupling distributions on the Anninghe-zemuhe-daliangshan-xiaojiang fault zone, southeastern Tibeatan plateau, based on GPS measurements. J Asian Earth Sci 219(3):104899. https://doi.org/104899.10.1016/j.jseaes.2021.104899

Li W, Chen Y, Yuan XH, Xiao WJ, Windley BF (2022) Intracontinental deformation of the Tianshan Orogen in response to India-Asia collision. Nat Commun 13(1):3738. https://doi.org/10.1038/s41467-022-30795-6

McCaffrey R (2005) Block kinematics of the Pacific–North America plate boundary in the southwestern United States from inversion of GPS, seismological, and geologic data. J Geophys Res Solid Earth 110(B7). https://doi.org/10.1029/2004JB003307

Meade BJ, Hager BH (2005) Block models of crustal motion in southern California constrained by GPS measurements. J Geophys Res 110(B3):1–19. https://doi.org/10.1029/2004JB003209

Okada Y (1985) Surface deformation due to shear and tensile faults in a half-space. B Seismol Soc Am 75(4):1135–1154

Pang YJ (2022) Stress evolution on major faults in Tien Shan and implications for seismic hazard. J Geodyn s 153–154

Parsons T (2006) Tectonic stressing in California modeled from GPS observations. J Geophys Res Solid Earth 111. https://doi.org/10.1029/2005JB003946

Paul S (2010) Earthquake and volcano deformation. Princeton University Press, Princeton

Riguzzi F, Crespi M, Devoti R, Doglioni C, Pietrantonio G, Pisani AR (2012) Geodetic strain rate and earthquake size: new clues for seismic hazard studies. Phys Earth Planet in 206:67–75. https://doi.org/10.1016/j.pepi.2012.07.005

Savage JC, Burford RO (1973) Geodetic determination of relative plate motion in central California. J Geophys Res 78(5):832–845. https://doi.org/10.1029/JB078i005p00832

Shan B, Xiong X, Wang R, Zheng Y, Yang S (2003) Coulomb stress evolution along Xianshuihe-Xiaojiang fault system since 1713 and its interaction with Wenchuan earthquake, May 12, 2008. Earth Planet Sc Lett 377(5):199–210

Shen ZK, Lü JN, Wang M, Brügmann R (2005) Contemporary crustal deformation around the southeast borderland of the Tibetan Plateau. J Geophys Res 110:B11409. https://doi.org/10.1029/2004JB003421

Shen ZK, Jackson DD, Kagan YY (2007) Implications of geodetic strain rate for future earthquakes, with a five-year forecast of M5 earthquakes in southern California. Seismol Res Lett 78(1):116–120. https://doi.org/10.1785/gssrl.78.1.116

Tape C, Muse P, Simons M, Dong D, Webb F (2009) Multiscale estimation of GPS velocity fields. Geophys J Int 179(2):945–971. https://doi.org/10.1111/j.1365-246X.2009.04337.x

Wang M, Shen ZK (2020) Present-day crustal deformation of continental China derived from GPS and its tectonic implications. J Geophys Res Solid Earth 125 e2019J B018774. https://doi.org/10.1029/2019JB018774

Wang YZ, Wang EN, Shen ZK, Wang M, Gan WJ, Qiao XJ, Meng GJ, Li TM, Tao Y, Yang YL (2008) Inversion of current movement velocity of Sichuan-Yunnan main rupture constrained by GPS data. Sci China (Series D: Earth Science) 38(5):582–597 (In Chinese with English abstract)

Wen XZ, Ma SL, Xu XW, He YN (2008) Historical pattern and behavior of earthquake ruptures along the eastern boundary of the Sichuan-Yunnan faulted-block, southwestern China. Phys Earth Planet in 168(4):16–36. https://doi.org/10.1016/j.pepi.2008.04.013

Wu YQ (2012) Research on the three-dimensional manifold method and its preliminary application to geosciences. Institute of Earthquake Forecasting, Beijing, pp P9–12

Wu YQ, Jiang ZS, Yang GH, Wei WX, Liu XX (2011) Comparison of GPS strain rate computing methods and their reliability. Geophys J Int 2703–717. https://doi.org/10.1111/j.1365-246X.2011.04976.x

Wu YQ, Jiang ZS, Liu XX, Wei WX, Zhu S, Zhang L, Zou ZY, Xiong XH, Wang QX, Du JL (2017) A comprehensive study of gridding methods for GPS horizontal velocity fields. Pure Appl Geophys 174(3):1201–1217. https://doi.org/10.1007/s00024-016-1456-z

Wu YQ, Jiang ZS, Guo BF, Yang GH, Bo WJ, Chang L, Li LY, Zhu S, Zhan W, Zheng ZJ, Liang HB (2021) Joint adjustment for large–area, multi–source vertical data: method, validation and application. Acta Geod Geophys 56:113–131. https://doi.org/10.1007/s40328-020-00328-y

Wu YQ, Jiang ZS, Pang YJ, Chen CY (2022) Statistical correlation of seismicity and geodetic strain rate in the chinese mainland. Seismol Res Lett 93:268–276. https://doi.org/10.1785/0220200048

Xu PL, Liu JN (2014) Variance components in errors-in-variables models: estimability, stability and bias analysis. J Geod 88:719–734. https://doi.org/10.1007/s00190-014-0717-9

Yu ZT, Lu LC (1978) Basis of surveying adjustment. Surveying and Mapping Press, Beijing

Zeng Y, Petersen MD, Shen ZK (2018) Earthquake potential in California-Nevada implied by correlation of strain rate and seismicity. Geophys Res Lett 45. https://doi.org/10.1002/2017GL075967

Zhan SH, Wang H, Zhou BY, Wu XW (2021) Shallow seismicity forecast for the Sichuan-Yunnan area based on geodetic strain rates. Urban Geotech Invest Surveying, (1):110–114 (In Chinese with English abstract)

Zhang SP (2019) Research on block fault activity in Sichuan-Yunnan region under the constraints of GPS result. Institute of Seismology, CEA, Beijing

Zhang QY, Wu YQ, Guo NN, Chen CY (2022) Research on deformation characteristics of the 2021 Qinghai Maduo Ms7.4 earthquake through coseismic dislocation inversion. Adv Space Res 69(8):3059–3070. https://doi.org/10.1016/j.asr.2022.01.042

Zhao J (2012) Analysis of block strain and fault zone deformation characteristics in Sichuan-Yunnan region using block derformation model and negative dislocation model. Institute of Earthquake Science, CEA, Beijing

Zheng G, Lou Y, Wang H, Geng JH, Shi C (2018) Shallow seismicity forecast for the India-Eurasia collision zone based on geodetic strain rates. Geophys Res Lett 45. https://doi.org/10.1029/2018GL078814